Niobium addition enhancing the corrosion resistance of nanocrystalline Ti$_5$Si$_3$ coating in H$_2$SO$_4$ solution

J. Xu [a,b,*], L. Liu [a], Z. Li [c], P. Munroe [d], Z.-H. Xie [e]

[a] Department of Material Science and Engineering, Nanjing University of Aeronautics and Astronautics, 29 Yudao Street, Nanjing 210016, People's Republic of China
[b] School of Mechanical & Electrical Engineering, Wuhan Institute of Technology, 693 Xiongchu Avenue, Wuhan 430073, People's Republic of China
[c] Institute of Mechanics, Chinese Academy of Sciences, Beijing 100190, People's Republic of China
[d] School of Materials Science and Engineering, University of New South Wales, NSW 2052, Australia
[e] School of Mechanical Engineering, University of Adelaide, SA 5005, Australia

Abstract

In this paper, novel Nb-containing Ti$_5$Si$_3$ (i.e., Ti$_{56.2}$Nb$_{6.3}$Si$_{37.5}$ and Ti$_{50.0}$Nb$_{12.5}$Si$_{37.5}$) nanocrystalline coatings were deposited onto Ti–6Al–4V substrates by a double glow discharge plasma technique. The effects of Nb alloying on the electrochemical behavior of the Ti$_5$Si$_3$ nanocrystalline coatings were systematically investigated in a naturally aerated 5 wt.% H$_2$SO$_4$ solution, for which various electrochemical techniques, including potentiodynamic polarization, electrochemical impedance spectroscopy (EIS), potentiostatic polarization and Mott–Schottky analysis, were employed. Moreover, to evaluate the corrosion performance of the as-deposited coatings over an extended period, their corrosion resistance was analyzed after 7 days' immersion in a 5 wt.% H$_2$SO$_4$ solution by EIS measurements and observations of corroded surface morphologies. The results showed that the Ti$_{62.5-x}$Nb$_x$Si$_{37.5}$ ($x = 0$, 6.3, 12.5) nanocrystalline coatings exhibit superior corrosion resistance compared with Ti–6Al–4V, and their corrosion resistance is enhanced with increasing Nb content, suggesting that Nb alloying is an effective strategy for improving the corrosion protection ability of the Ti$_5$Si$_3$ nanocrystalline coating. The roles of Nb additions in enhancing the corrosion resistance of the Ti$_5$Si$_3$ nanocrystalline coatings can be summarized as: (a) reducing the residual tensile stresses of the as-deposited coatings and (b) tailoring the composition, compactness and electronic structure of the passive films formed. These findings are expected to broaden the application of Ti$_5$Si$_3$ as a highly corrosion-resistant coating for engineering components operating under aggressive conditions.
© 2013 Acta Materialia Inc. Published by Elsevier Ltd. All rights reserved.

Keywords: Nanocrystalline film; Sputter deposition; Electrochemical impedance; Corrosion; Transition-metal silicides

1. Introduction

Titanium alloys are relatively new engineering materials, possessing an extraordinary combination of properties, such as high specific strength, good corrosion resistance and biocompatibility. They are commonly used in aerospace structures, space vehicles and medical devices, and in the petroleum and chemical industries [1,2]. The excellent corrosion resistance of titanium alloys in many industrial environments arises from the existence of a protective oxide film that forms naturally upon exposure to air [3]. However, titanium alloys exhibit low corrosion resistance in strong reducing acids such as sulfuric acids, which has restricted their use for safety–critical applications [4]. Furthermore, under the application of static or dynamic contact loads, the thin passive film would be easily destroyed. Because bare titanium alloys have a strongly negative standard electrode potential (-1.63 V), they often suffer galvanic and crevice corrosion as well as corrosion

embrittlement caused by intensive interactions with the interface material and/or the surrounding environment [5]. In the past decade, various surface modification techniques, including micro-plasma oxidation [6], laser treatment [7], chemical vapor deposition [8], physical vapor deposition [9] and ion implantation [10], have been developed to improve the resistance of titanium alloys against abrasion and corrosion damage. Among these methods, the application of a double glow discharge plasma technique, through the synthesis of nanocrystalline transition metal silicide coatings, has proved to be an economical and effective way to enhance the surface properties of titanium alloys [11,12].

As a promising high-temperature engineering material, Ti_5Si_3 has recently attracted much interest because of its high melting temperature (2130 °C), low density (4.32 g cm^{-3}), excellent creep strength and high oxidation resistance [13,14]. Moreover, highly covalent-dominated atomic bonds endow Ti_5Si_3 with good chemical inertness and high hardness, which has generated vigorous pursuit of Ti_5Si_3 as a wear- and corrosion-resistant coating material. Unfortunately, since Ti_5Si_3 has a hexagonal crystal structure, the thermal expansion anisotropy, originating from a large difference between the coefficients of thermal expansion (CTE) in the crystallographic c and a directions (CTE(c)/CTE(a) ratios of ∼3), results in appreciable residual stresses in the material during heating and cooling that can give rise to microcracking [15,16]. To alleviate or eliminate this problem, alloying by substitutional elements, which acts to change the chemical bond nature and/or refine the crystal size, has been performed to control the degree of strain or microcracking. For example, Thom et al. [17] suggested that a critical grain size of pure Ti_5Si_3 and carbon-containing Ti_5Si_3 is 2–3 μm and 5–6 μm, respectively, needed to completely avoid microcracking. Experimental observations also indicated that the thermal-expansion anisotropy of Ti_5Si_3 exhibits a substantial reduction by replacing some of the titanium by zirconium, niobium or chromium [18,19]. It is worth noting that previous studies focused mainly on physical and mechanical properties, with little attention devoted to understanding the electrochemical behavior of Ti_5Si_3 in aqueous corrosive environments. In an earlier study, the present authors investigated the influence of carbon addition on the electrochemical characteristics of Ti_5Si_3, and found that the small additions of carbon have a significantly positive impact on the corrosion resistance of Ti_5Si_3 in 3.5 wt.% NaCl solution [20]. Considering the fact that Nb not only has a high solubility in Ti_5Si_3 (∼21 at.%), but also possesses high passivating ability in diverse aqueous environments [21,22], it is hypothesized that Nb could be a desirable additive to Ti_5Si_3, which acts to reduce both the residual tensile stress and tailor the surface properties of Ti_5Si_3 and, consequently, enhance its corrosion resistance.

To test this hypothesis, two Nb-containing Ti_5Si_3 coatings (i.e., $Ti_{56.2}Nb_{6.3}Si_{37.5}$ and $Ti_{50.0}Nb_{12.5}Si_{37.5}$) were prepared by a double glow discharge plasma technique. The microstructure of the as-deposited coatings was first

characterized by X-ray diffraction (XRD), scanning electron microscopy (SEM), energy-dispersive X-ray spectroscopy and transmission electron microscopy (TEM). Subsequently, the electrochemical behavior of the coatings was investigated by potentiodynamic polarization, electrochemical impedance spectroscopy (EIS), potentiostatic polarization and capacitance measurement (Mott–Schottky approach) in a naturally aerated 5 wt.% H_2SO_4 solution. In addition, X-ray photoemission spectroscopy (XPS) was employed to identify the composition and chemical bonding states of the passive films grown on the coatings following potentiostatic polarization tests. For comparative purposes, these measurements were also performed on a Ti_5Si_3 nanocrystalline coating and the uncoated Ti–6Al–4V substrate. Finally, the roles of Nb additions in governing the corrosion mechanisms of the Ti_5Si_3 coatings were elucidated.

2. Experimental

2.1. Specimen preparation

Disk-shaped substrates, 40 mm in diameter and 3 mm thick, were machined from a commercial Ti–6Al–4V alloy rod. The nominal composition of this alloy in weight per cent is: Al, 6.04; V, 4.03; Fe, 0.3; O, 0.1; C, 0.1; N, 0.05; H, 0.015 and the balance Ti. Prior to coating deposition, the substrates were successively ground with a series of silicon carbide papers and finally polished with 1.5 μm diamond paste to obtain a mirror-like surface finish. The polished substrates were then ultrasonically cleaned in ethyl alcohol and dried in cold air. Three types of coatings—$Ti_{62.5}Si_{37.5}$ (i.e., Ti_5Si_3 as a reference), $Ti_{56.2}Nb_{6.3}Si_{37.5}$ and $Ti_{50.0}Nb_{12.5}Si_{37.5}$—were deposited onto the polished substrates by a double cathode glow discharge technique, using three targets with different stoichiometric ratios ($Ti_{50}Si_{50}$, $Ti_{45}Nb_5Si_{50}$ and $Ti_{40}Nb_{10}Si_{50}$, respectively). The targets were fabricated from ball-mill Ti (−300 mesh, 99.9% purity), Nb (−300 mesh, 99.9% purity), and Si (−200 mesh, 99.5% purity) by employing cold compaction under a pressure of 600 MPa. During the deposition process, one cathode was the target composed of the desired sputtering materials, and the other was the substrate. When voltages were applied to the two cathodes, glow discharge occurred, as described elsewhere [20]. The glow discharge sputtering parameters can be described as follows: base pressure, 5×10^{-3} Pa; working pressure, 35 Pa; target–substrate distance, 10 mm; target electrode bias voltage, −800 V; substrate electrode bias voltage, −300 V; substrate temperature, 800 °C; and treatment time, 3 h.

2.2. Microstructure characterization and composition analysis

The phase compositions of the as-deposited coatings were characterized by X-ray diffractometry (XRD; D8 ADVANCE with Cu Kα radiation) operating at 35 kV

and 40 mA. X-ray spectra were collected in the 2θ range from 20° to 90° with a scan rate of 0.5° min^{-1}. The cross-sectional microstructural features and chemical composition of the as-prepared coatings were examined by field emission scanning electron microscopy (FESEM; Hitachi, S-4800, Japan) equipped with energy-dispersive X-ray spectrometry (EDS). The sectioned coatings were etched using Kroll's reagent (1% HF, 2% HNO$_3$ and 97% H$_2$O) for 1 min to obtain good visibility of the coating/substrate interface. TEM was performed using a JEOL JEM-2010 microscope operated at an accelerating voltage of 200 kV. Plane-view samples for TEM observation were prepared by single-jet electrochemical polishing from the untreated side of the substrate. XPS measurements were carried out using a Kratos AXIS Ultra ESCA system with an Al Kα (1486.71 eV) X-ray source. The accelerating voltage and emission current of the X-ray source were kept at 12 kV and 12 mA, respectively. The base pressure of the sample analysis chamber was maintained at $\sim10^{-10}$ Torr. The pass energy was selected at 80 eV for survey scan and 10 eV for the features of interests (i.e., Ti $2p$, Nb $3d$ and Si $2p$) to ensure high resolution and good sensitivity. The quantitative analysis of XPS experimental data was carried out using CasaXPS-Version 2.3.14. Shirley background type was employed for background subtraction for each high-resolution spectrum. The decoupling of spectra was performed using Gaussian function with zero asymmetry index. The relative sensitivity factors for each element were obtained from the standard database of CasaXPS. The atomic concentration of each component was determined based on the percentage area of the component calculated by Casa XPS software.

2.3. Electrochemical studies

A standard three-electrode system consisting of a Pt counter-electrode, a saturated calomel reference electrode and a working electrode made from a specimen with a 1.0 cm^2 exposed area was employed to carry out the electrochemical measurements. Throughout this work, potentials were measured with respect to the saturated calomel electrode (SCE). All electrochemical measurements were conducted at room temperature, using an electrochemical workstation (CHI 660C, Shanghai, China) in naturally aerated 5 wt.% H$_2$SO$_4$ solution prepared with analytical grade reagent and distilled water. Prior to the electrochemical experiment, the working electrode was reduced potentiostatically at -0.80 V for 10 min to remove air-formed oxides. The potentiodynamic polarization curves were recorded at a scan rate of 1.0 mV s^{-1}, starting from the moment when the open circuit potential (OCP) reached its steady state (usually occurring after the specimen had been immersed in the electrolyte for ~30 min). The EIS measurements were carried out using an excitation signal of 10 mV peak-to-peak over a frequency range from 100 kHz extending up to 10 mHz at the respective OCP. The EIS experimental data were analyzed and fit to appropriate electrical equivalent circuit (EEC) using the ZSimpWin software. Capacitance measurements for Mott–Schottky analysis were conducted after the specimens had been potentiostatically polarized at a passive potential of 0.80 V for 1 h to form a steady-state passive film. Subsequently, the capacitance of passive film covered specimen was measured at a fixed frequency of 1000 Hz by stepping the potential in the cathodic direction from the film formation potential (0.80 V) to -0.20 V in 25 mV increments. This method assumes that the thickness and structure of the passive film and the defect concentration are "frozen-in", while the electronic structure responds to the changing potential. Each type of electrochemical measurement was repeated at least three times to ensure reproducibility.

2.4. Theoretical models and computational details

First-principles calculations were performed based on the plane wave pseudopotential within the density functional theory, using the Cambridge Serial Total Energy Package [23]. The interactions between the ionic cores and the electrons were defined by the ultrasoft pseudopotentials, and the orbital electrons of Ti-3$d^2$4s^2, Si-3$s^2$3p^2 and Nb-4$d^5$5s^1 were treated as valence electrons. The exchange and correlation terms were treated with the Perdew–Burke–Ernzerh functional in the generalized gradient approximation scheme [24]. An energy cutoff of 400 eV and a $4 \times 4 \times 6$ k point mesh generated by the Monkhorst–Pack method [25] were used for all the calculations.

For unalloyed Ti$_5$Si$_3$, the calculation was performed on a 16-atom unit cell containing two chemical formulas of Ti$_5$Si$_3$, as shown in Fig. 1. In the case of Nb alloyed Ti$_5$Si$_3$, the crystal structure of ternary Ti$_{62.5-x}$Nb$_x$Si$_{37.5}$ remains the same as unalloyed Ti$_5$Si$_3$. To generate compositions close to experimental stoichiometries, the Ti$_{62.5-x}$Nb$_x$Si$_{37.5}$ crystal structures were constructed using the above model, wherein Ti atoms were replaced by 1 and 2 Nb atoms and the corresponding Nb concentrations (i.e., 'x' value) were 6.25 and 12.50, respectively. The crystal structures of Ti$_{62.5-x}$Nb$_x$Si$_{37.5}$ were optimized using the Broyden–Fletcher–Goldfarb–Shanno minimization method [26]. Both lattice parameters and atomic coordinates were relaxed until the total energy tolerance was $<5.0 \times 10^{-6}$ eV atom^{-1}, the maximum ionic Hellmann–Feynman force within 0.01 eV Å^{-1}, the maximum ionic displacement within 5.0×10^{-4} Å, and the maximum stress within 0.02 GPa. The Young's modulus for binary and ternary Ti$_5$Si$_3$ with a D8$_8$ hexagonal structure was calculated based on the Voigt–Reuss–Hill approximation [27].

3. Results

3.1. Phase composition and residual stress analysis

Fig. 2 presents the XRD patterns recorded from the binary Ti$_5$Si$_3$ and ternary Ti$_{56.2}$Nb$_{6.3}$Si$_{37.5}$ and Ti$_{50.0}$Nb$_{12.5}$Si$_{37.5}$ coatings, together with the powder diffraction file data for
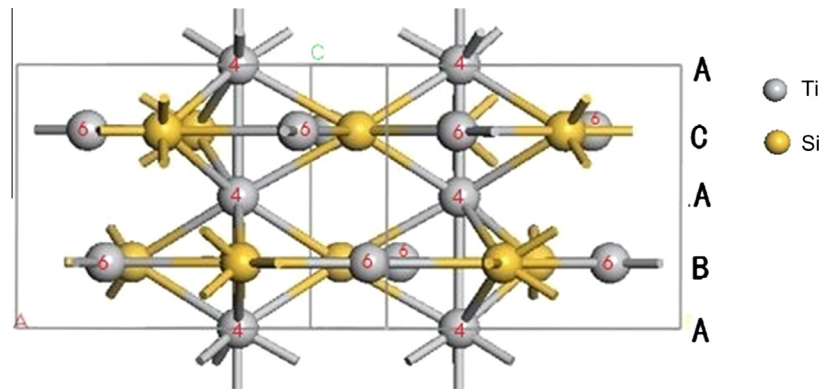
Fig. 1. Calculation unit cell of three Ti_5Si_3 in $D8_8$ crystal structure. Ti atoms with a number of 4 and 6 denote Ti^{4d} and Ti^{6g}, respectively.

Ti_5Si_3 (represented by vertical dotted lines). All the diffraction peaks of the three coatings can be indexed to the hexagonal $D8_8$-structured Ti_5Si_3 phase (JCPDS Card No. 29-1362). In comparison with the data in JCPDS card No. 29-1362, the peak positions for the Ti_5Si_3 phase shift slightly towards higher angles for the Ti_5Si_3 coating, indicative of the presence of residual tensile stresses in the coating. However, with increasing Nb content, the peak positions of Ti_5Si_3 for the two Nb-containing Ti_5Si_3 nanocrystalline coatings shift to lower 2θ values compared with those of the monolithic Ti_5Si_3 coating. This phenomenon might be due to both Nb atoms being present in solid solution in the Ti_5Si_3 phase and also a reduction in the residual tensile stresses in the coatings. Because Nb and Ti in the periodic table belong to the VB and IVB group, respectively, they have similar chemical properties. The atomic sizes of Ti and Nb are also very similar (Ti = 0.145 nm and Nb = 0.148 nm). Therefore, Nb atoms can dissolve into Ti_5Si_3 and occupy Ti sites, forming a substitutional solid solution. Zhang and Wu [28] reported that the solubility of Nb in Ti_5Si_3 was determined as at least 21 at.% during casting. One could speculate that the shift in the diffraction peaks for ternary $Ti_{56.2}Nb_{6.3}Si_{37.5}$ and $Ti_{50.0}Nb_{12.5}Si_{37.5}$ coatings may originate predominantly from a decrease in residual stress after the incorporation of Nb into Ti_5Si_3.

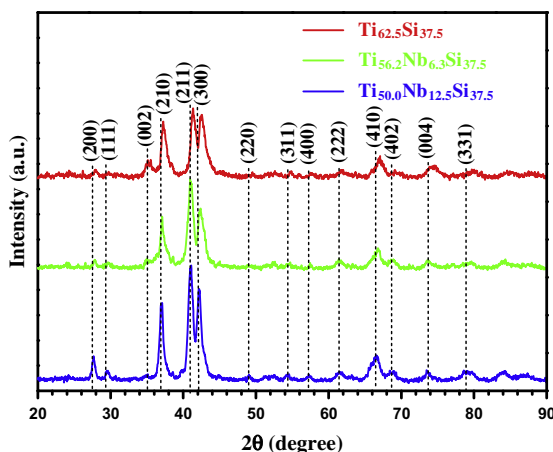In order to further explore and quantify the residual stresses in the as-deposited coatings, the lattice parameters, Young's modulus and Poisson's ratio of the $D8_8$-structured $Ti_{62.5-x}Nb_xSi_{37.5}$ ($x = 0$, 6.25, 12.50) were calculated by first-principles calculations. Table 1 summarizes the lattice constants, Young's modulus and Poisson's ratio for the $D8_8$-structured $Ti_{62.5-x}Nb_xSi_{37.5}$ ($x = 0$, 6.25, 12.50). After deduction of the contribution of composition dependence to the observed d-spacing for $Ti_{62.5-x}Nb_xSi_{37.5}$, a rough estimation of the residual stresses in the as-deposited nanocrystalline coatings can be determined using the following expression [29]:

$$\sigma = -\frac{E}{v}\left(\frac{d_n - d_0}{d_0}\right) \tag{1}$$

where E, v, d_n and d_0 are, respectively, the Young's modulus, Poisson's ratio, d-spacing of the $(2\,1\,1)$ plane obtained from the experimental value and the calculated value as a strain-free reference. The results show that the three coatings exhibit residual tensile stresses in the range 2.2–7.7 GPa, which decrease with increasing Nb content. It is worth noting that the internal stress state within a coating plays an important role in governing the corrosion resistance of the coating [30], and an adverse tensile stress state could lead to inferior resistance to corrosion attack in a manner analogous to stress corrosion cracking in metals [31,32]. Owing to its hexagonal crystal structure, Ti_5Si_3 exhibits a large thermal expansion anisotropy that could result in high residual stresses in the resultant coating following high-temperature synthesis. Zhang and Wu [18] reported that alloying with Nb could significantly reduce the thermal expansion anisotropy of Ti_5Si_3, because the substitution of Nb for Ti alters the bonding states in the Ti_5Si_3 unit cell. As supported by the above calculated results, the residual tensile stress accumulated in the Ti_5Si_3 nanocrystalline coating was significantly reduced by Nb additions. This is expected to contribute to an improvement in its corrosion resistance.

3.2. Microstructure characterization

Fig. 3 shows cross-sectional SEM images and corresponding EDS spectra from the coatings. All coatings are

Fig. 2. Typical XRD patterns recorded from the as-deposited $Ti_{62.5}Si_{37.5}$, $Ti_{56.2}Nb_{6.3}Si_{37.5}$ and $Ti_{50.0}Nb_{12.5}Si_{37.5}$ nanocrystalline coatings.

Table 1
Calculated properties of binary and ternary Ti$_5$Si$_3$, including lattice parameters, Young's modulus (E), Poisson's ratio, d-spacing of the (211) plane obtained from the experiment (d_n) and calculated d-spacing of the (211) plane (d_0) and residual tensile stresses.

Sample	a (Å)	c (Å)	E (GPa)	v	d_0 (Å)	d_n (Å)	σ (GPa)
Ti$_{62.5}$Si$_{37.5}$	7.4662	5.1247	235.90	0.222	2.2050	2.1892	7.61
Ti$_{56.25}$Nb$_{6.25}$Si$_{37.5}$	7.4877	5.1506	236.13	0.225	2.2131	2.2026	4.98
Ti$_{50.0}$Nb$_{12.5}$Si$_{37.5}$	7.5066	5.1743	237.26	0.230	2.2197	2.2149	2.23

tightly adhered to the Ti–6Al–4V substrate and exhibit dense structures with neither voids nor microcracks visible across the breadth of the coatings. The microstructure of these three coatings consists of two sublayers; namely, the ~10 μm thick outer deposition layer and an inner diffusion layer with thickness ~2 μm. EDS analysis shows that the outer layers have a Si/Ti or Si/(Ti + Nb) atomic ratio approaching the ideal value of 0.6 for the theoretical Si/Ti or Si/(Ti + Nb) atomic ratio in Ti$_5$Si$_3$ or (Ti, Nb)$_5$Si$_3$, indicating that the outer layers of the three coatings are composed of single phase Ti$_5$Si$_3$ or (Ti, Nb)$_5$Si$_3$. Analytical and high-resolution TEM (HRTEM) analysis provide further details about the microstructural characteristics of the outer layer of the as-deposited coatings. Fig. 4a shows a plan-view TEM bright-field image of the outer layer captured from the Ti$_{50.0}$Nb$_{12.5}$Si$_{37.5}$ coating. Clearly, its outer layer consists of cauliflower-like constituents with an average diameter of 180 nm, which bears a striking resemblance to the microstructural features found in the Ti$_5$Si$_3$ nanocrystalline coating, as described elsewhere [20]. Selected-area electron diffraction (SAED) (Fig. 4b) shows a ring pattern consistent with the (2 1 0), (3 0 0), (2 2 2) and (4 1 0) lattice planes of hexagonal D8$_8$-structured Ti$_5$Si$_3$. In addition, the high-magnification TEM image (Fig. 4c) reveals that the cauliflower-like domains are composed of petal-like Ti$_5$Si$_3$ grains with an average size of ~15 nm. A high-resolution lattice image from a selected petal in Fig. 4d and corresponding fast Fourier transform (FFT) pattern (inset) shows that the spacing of the lattice fringes is 0.325 nm, which is close to the {2 0 0} planes spacing of the hexagonal Ti$_5$Si$_3$ phase.

3.3. Potentiodynamic polarization tests

Fig. 5a shows the representative potentiodynamic polarization curves of the two Nb-containing Ti$_5$Si$_3$ nanocrystalline coatings (i.e., Ti$_{56.2}$Nb$_{6.3}$Si$_{37.5}$ and Ti$_{50.0}$Nb$_{12.5}$Si$_{37.5}$) in comparison with those of the Ti$_5$Si$_3$ nanocrystalline coating and the uncoated Ti–6Al–4V substrate obtained in naturally aerated 5 wt.% H$_2$SO$_4$ solution at room temperature. The values of the related electrochemical parameters, i.e., corrosion potential (E_{corr}), corrosion current density (i_{corr}), passive current density (i_{pass}) and anodic (β_a) and cathodic (β_c) Tafel slopes were determined from the polarization curves and are summarized in Table 2. Additionally, it is evident from Fig. 5a that all the tested specimens are spontaneously passivated in the solution, as indicated by no observable active/passive transient peaks in all the curves.

Compared with the uncoated Ti–6Al–4V substrate, the anodic and cathodic branches of the three coatings move simultaneously towards lower current densities, denoting that the anodic reaction and cathodic hydrogen evolution reaction of the three coatings occur with more difficulty. From Table 2, the cathodic Tafel slopes (β_c) of the tested specimens are very close, in the range −121.20 to −97.84 mV dec^{-1}, whereas the anodic Tafel slopes (β_a) of the three coatings are considerably larger than that for the uncoated Ti–6Al–4V substrate. According to the mixed potential theory (Fig. 5b), the cathodic and anodic branches shift following the order c0 → c1 → c2 → c3 and a0 → a1 → a2 → a3, respectively, for the uncoated Ti–6Al–4V substrate, the Ti$_5$Si$_3$, Ti$_{56.2}$Nb$_{6.3}$Si$_{37.5}$ and Ti$_{50.0}$Nb$_{12.5}$Si$_{37.5}$ nanocrystalline coatings. Such variations result in a positive shift for E_{corr} and a decreased i_{corr}, as shown in Table 2. With the increase in Nb content, the corrosion potential (E_{corr}) continuously shifts in a positive direction, and both the corrosion current density (i_{corr}) and passive current density (i_{pass}) decreased, suggesting that the addition of Nb has a positive effect on the anticorrosion performance of Ti$_5$Si$_3$.

3.4. Electrochemical impedance spectroscopy measurements

EIS has been broadly employed for the study of electrochemical behavior of coated systems in aqueous corrosive environments [33–35]. By measuring the impedance response of specimens to small AC potentials, much information on the corrosion reaction, the mass transfer and the electrical charge transfer can be obtained. Furthermore, some important parameters associated with the passive film (or barrier layer), such as the ohmic resistance, capacitance and thickness, can be deduced and compared [36,37]. Fig. 6 represents the Nyquist and Bode plots of the two Nb-containing Ti$_5$Si$_3$ nanocrystalline coatings, the Ti$_5$Si$_3$ nanocrystalline coating and the uncoated Ti–6Al–4V substrate at respective OCP in naturally aerated 5 wt.% H$_2$SO$_4$ solution. The response for the uncoated Ti–6Al–4V substrate in the Nyquist complex plan is essentially a depressed semicircle. The presence of depressed semicircles, often referred to as frequency dispersion, has been attributed to high roughness and inhomogeneity of the electrode surface [38,39]. In contrast, the Nyquist plots of the three nanocrystalline coatings display flattened and incomplete capacitive arcs in the entire frequency range. Most notably, the complex plan plot of the Ti$_{50.0}$Nb$_{12.5}$Si$_{37.5}$ nanocrystalline coating is almost a straight line, similar to that of platinum in
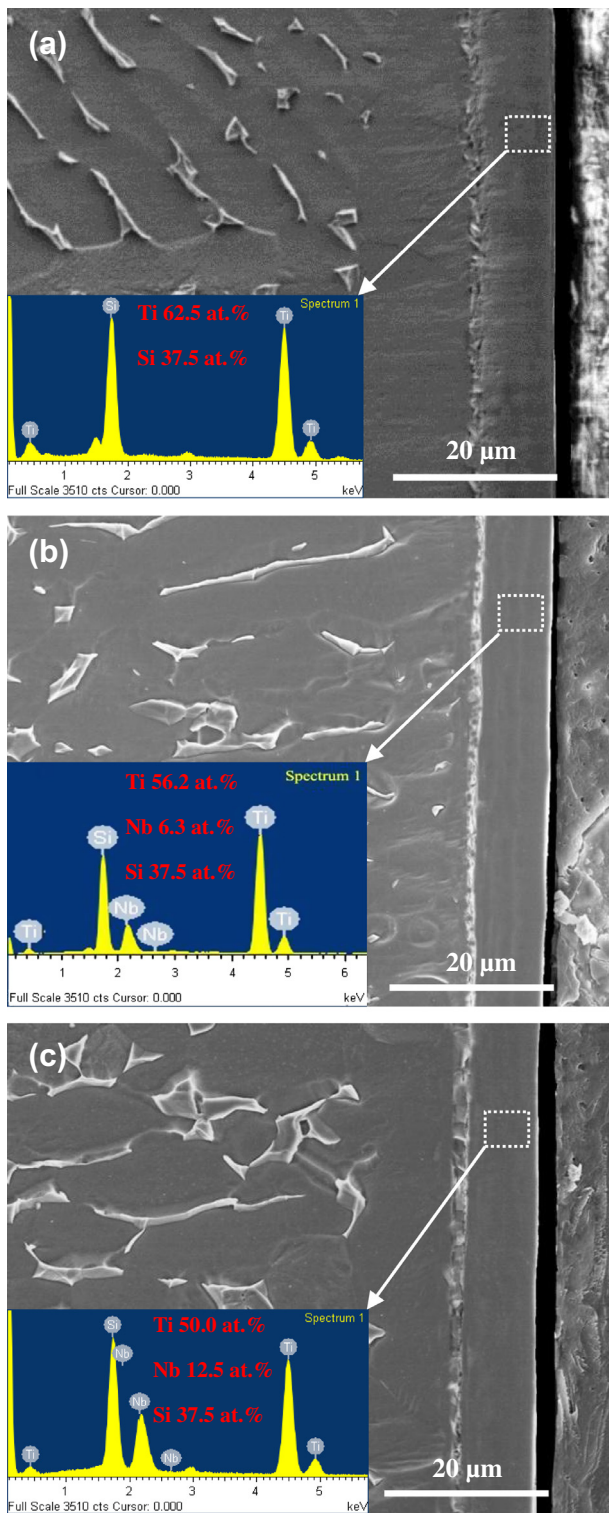
Fig. 3. Cross-sectional SEM morphologies and corresponding EDS spectra of (a) as-deposited $Ti_{62.5}Si_{37.5}$, (b) $Ti_{56.2}Nb_{6.3}Si_{37.5}$ and (c) $Ti_{50.0}Nb_{12.5}Si_{37.5}$ nanocrystalline coatings.

0.5 M H_2SO_4 solution [40], suggesting good insulating (dielectric) properties of the protective passive film formed on the specimen surface. It should also be noted that the curve for the Ti_5Si_3 coatings exhibits much larger diameters of semicircles than the uncoated Ti–6Al–4V substrate,

suggesting that the application of the coatings has greatly improved the corrosion resistance of Ti–6Al–4V. Further enhancement in the corrosion resistance of the Ti_5Si_3 nanocrystalline coating is achieved by the incorporation of Nb, as evidenced by the observation that the two Nb-containing Ti_5Si_3 nanocrystalline coatings yield larger semicircle diameters than the monolithic Ti_5Si_3 nanocrystalline coating. As shown in Fig. 6b, the Bode plot of the uncoated Ti–6Al–4V substrate shows the typical features of electrochemical reactions, characterized by a maximum near $-90°$ in the Bode-phase plot and two well-defined flat regions in the Bode-magnitude plot [41]. In the case of three Ti_5Si_3-based coatings, a strong capacitive behavior, typical of passive systems, is evident in a broad frequency range, with phase angles approaching $-90°$ and a slope of $\log|Z|$ vs. $\log f$ close to -1. It is suggested that the highly compact and stable passive films may be formed on the coating surface, especially in the $Ti_{50.0}Nb_{12.5}Si_{37.5}$ nanocrystalline coating.

In order to provide "quantitative support" to the experimental EIS results, impedance data were fitted to appropriate EEC using the ZSimpWin software. The equivalent circuit model with two hierarchically distributed time constants is generally used to describe coated systems [28,33,42,43]. In the present case, the wide phase angle maxima observed in the Bode plots of the three coatings validates the involvement of two overlapping time constants [43,44]. However, though the simulation results show excellent agreement with the experimental data using this treatment, the value for each of the constant phase elements (CPE) and the associated capacitances are of the same order of magnitude. Consequently, this makes it difficult to associate these parameters with the coating's response. Moreover, the errors for some of the elements comprising the circuit are very high ($\sim55.4\%$), leading to low confidence in their values. Therefore, a modified Randles circuit, shown in Fig. 7, was employed to obtain quantitative information on the electrochemical performance of the investigated specimens. The choice of this equivalent circuit represents a compromise between having a reasonable fit for the experimental values, limited by the software used, and maintaining the number of circuit elements at a minimum, and can relate these elements to the events occurring at the electrode. In this circuit, a CPE was used instead of a pure capacitance to take into consideration the distributed relaxation feature of the passive films so as to obtain a best fit. The impedance, Z_{CPE}, of CPE is defined by $Z_{CPE} = [Q(j\omega)^n]^{-1}$, where Q is the frequency independent parameter (Ω^{-1} cm^{-2} s^n), ω is the angular frequency (rad s^{-1}), j is the imaginary number, and the factor n, defined as a CPE power, is an adjustable parameter that always lies between 0.5 and 1. When $n = 1$, the CPE behaves as a pure capacitor; for $0.5 < n < 1$, the CPE describes a distribution of dielectric relaxation times in the frequency domain; and when $n = 0.5$, the CPE represents a Warburg impedance with diffusion character. The physical significance of the circuit elements is as follows:
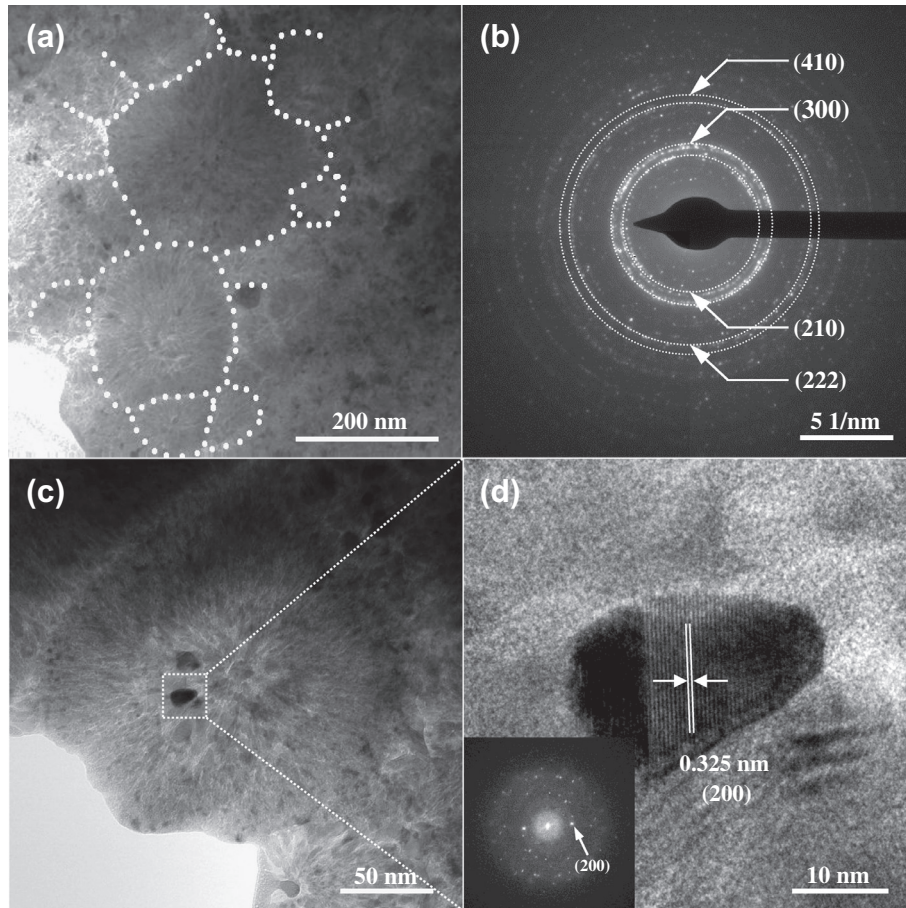
Fig. 4. Plan-view of (a) TEM bright-field image and (b) SAED pattern of the as-deposited $Ti_{50.0}Nb_{12.5}Si_{37.5}$ nanocrystalline coating; (c) local magnifying image and (d) HRTEM image of the cauliflower-like clustered domain in the $Ti_{50.0}Nb_{12.5}Si_{37.5}$ nanocrystalline coating. The inset in (d) is the FFT pattern of local cauliflower-like clustered growth domain.

R_s is the solution resistance, and CPE and R_p are the constant phase element and polarization resistance, respectively. Table 3 compiles the numerical values of circuit elements from the fitting procedure. The chi-squared (χ^2) values of the order of 10^{-3}–10^{-4} indicate satisfactory agreement between the experimental and simulated data. The parameter R_p, including the contributions of the charge-transfer resistance, the passive film resistance and the migration of point defects mediating the growth of the passive film and dissolution of metal through it, can be used to evaluate the corrosion resistance of the investigated specimens [45]. From Table 3, R_p increases from $4.65 \times 10^4\,\Omega\,cm^2$ for the Ti–6Al–4V substrate to $1.49 \times 10^6\,\Omega\,cm^2$ for Ti_5Si_3 coating and further to 3.55×10^6 and $4.36 \times 10^6\,\Omega\,cm^2$ for the specimen protected by the $Ti_{56.2}Nb_{6.3}Si_{37.5}$ and $Ti_{50.0}Nb_{12.5}Si_{37.5}$ nanocrystalline coating, respectively. Nearly two orders of magnitude improvement in R_p were achieved by implementation of the three Ti_5Si_3-based coatings. Considering the fact that the resistance values obtained from EIS data are highly dependent on the solution in which the measurements are made, the capacitance values are independent of the solution conditions and are therefore a much more

reliable means of determining electrochemical properties of electrode [36]. The values of effective capacitance (C) of the investigated specimens can be converted from CPE through the Brug approach [46], as described by Eq. (2).

$$C = Q^{1/n} \left(\frac{1}{R_s} + \frac{1}{R_p} \right)^{n-1/n} \tag{2}$$

The values of C for the Ti–6Al–4V substrate, Ti_5Si_3, $Ti_{56.2}Nb_{6.3}Si_{37.5}$ and $Ti_{50.0}Nb_{12.5}Si_{37.5}$ nanocrystalline coatings are, respectively, 38.38, 5.98, 4.92 and 4.49 $\mu F\,cm^{-2}$. Much lower values of C for the three coatings reflect higher insulating properties of the passive films formed on their surfaces compared with that grown on the uncoated Ti–6Al–4V substrate. Moreover, the time constant (τ), expressed as $\tau = C \times R_p$, can be used to describe the rate of relevant electrochemical process [47]. As shown in Table 3, the τ values of the two Nb-containing nanocrystalline coatings are significantly larger than that of the Ti_5Si_3 coating and about one order of magnitude greater than that of the uncoated Ti–6Al–4V substrate, indicating that the presence of Nb has an obvious retarding effect on the electrochemical corrosion process of the Ti_5Si_3 nanocrystalline coating.

(a)

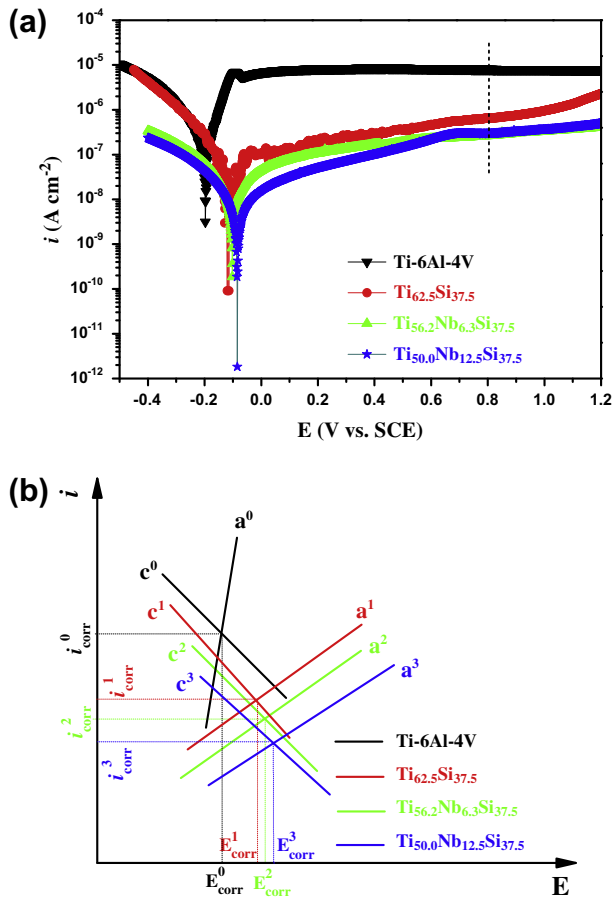**(b)**

Fig. 5. (a) Representative potentiodynamic polarization curves for the two Nb-containing Ti_5Si_3 nanocrystalline coatings, Ti_5Si_3 nanocrystalline coating and the uncoated Ti–Al–4V alloy in a naturally aerated 5 wt.% H_2SO_4 solution; (b) Mixed potential theory applied to schematically interpret the changes in E_{corr} and i_{corr}. Curve a is for the anodic semireaction, and curve c is for the cathodic semireaction.

3.5. Immersion tests

To investigate the effect of Nb alloying on the corrosion resistance of the coated specimens in naturally aerated 5 wt.% H_2SO_4 solution over an extended period of time, EIS measurements and corroded surface examinations were conducted. Fig. 8 presents the impedance spectra of the three as-deposited nanocrystalline coatings and the uncoated Ti–Al–4V substrate after immersion for 7 days in 5 wt.% H_2SO_4 solution. In comparison with the impedance response shown in Fig. 6, no significant change in

(a)

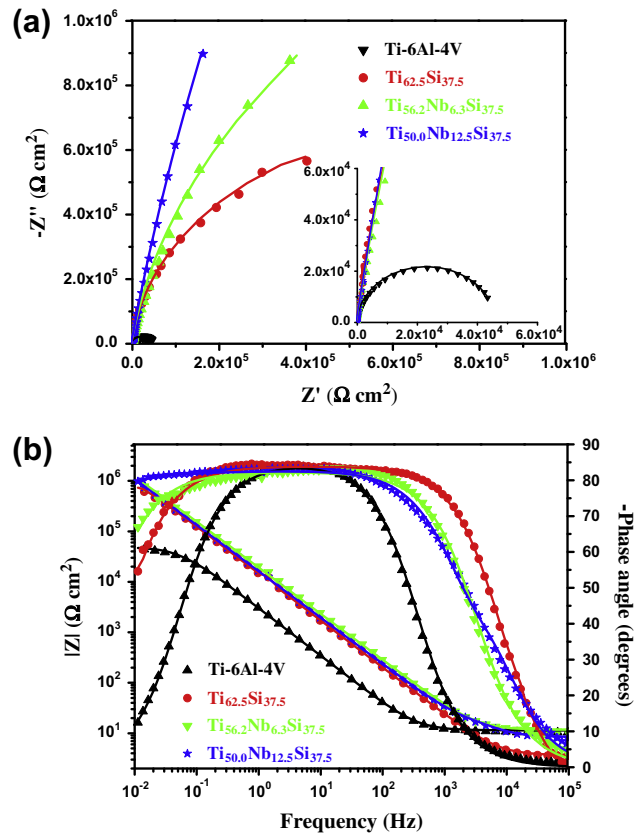**(b)**

Fig. 6. (a) Nyquist and (b) Bode plots of the two Nb-containing Ti_5Si_3 nanocrystalline coatings, the Ti_5Si_3 nanocrystalline coating and the uncoated Ti–6Al–4V substrate at respective OCP in a naturally aerated 5 wt.% H_2SO_4 solution. Symbols are experimental data and solid lines are fitting results.
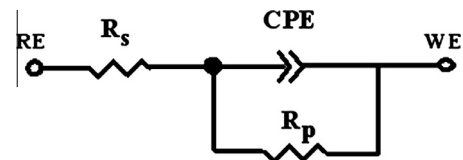

Fig. 7. Electronic equivalent circuit used in the fitting procedure of the EIS data.

impedance behavior is detectable for the two Nb-containing Ti_5Si_3 nanocrystalline coatings after the immersion, as shown by the diameter of capacitance semicircle and the phase angle maximum. This indicates that the two Nb-containing Ti_5Si_3 nanocrystalline coatings have

Table 2
Electrochemical parameters extracted from potentiodynamic polarization curves of investigated specimens in a naturally aerated 5 wt.% H_2SO_4 solution.

Samaples	Ti–6Al–4V	$Ti_{62.5}Si_{37.5}$	$Ti_{56.2}Nb_{6.3}Si_{37.5}$	$Ti_{50.0}Nb_{12.5}Si_{37.5}$
E_{corr} (V vs. SCE)	−0.20	−0.12	−0.10	−0.08
β_a (mV/decade)	58.01	208.46	233.32	243.37
$-\beta_c$ (mV/decade)	111.11	97.84	119.64	121.20
i_{corr} (A cm^{-2})	9.63×10^{-7}	3.10×10^{-8}	2.02×10^{-8}	9.41×10^{-9}
i_{pass}[a] (A cm^{-2})	8.07×10^{-6}	6.49×10^{-7}	2.84×10^{-7}	2.92×10^{-7}

[a] The passive current densities were derived at 0.80 V vs. SCE.

Table 3
Electrochemical parameters derived from impedance fitting for investigated specimens in a naturally aerated 5 wt.% H_2SO_4 solution.

Samples	Ti–6Al–4V	Ti$_{62.5}$Si$_{37.5}$	Ti$_{56.2}$Nb$_{6.3}$Si$_{37.5}$	Ti$_{50.0}$Nb$_{12.5}$Si$_{37.5}$
R_s (Ω cm^2)	10.74 ± 0.04	3.51 ± 0.04	10.97 ± 0.12	8.00 ± 0.09
CPE ($\times 10^{-6}$ Ω^{-1} cm^{-2} s^n)	58.97 ± 0.29	12.37 ± 0.06	11.35 ± 0.10	11.88 ± 0.02
n	0.945 ± 0.001	0.933 ± 0.001	0.915 ± 0.002	0.905 ± 0.003
R_p (Ω cm^2)	$(4.65 \pm 0.04) \times 10^4$	$(1.49 \pm 0.05) \times 10^6$	$(3.55 \pm 0.11) \times 10^6$	$(4.36 \pm 0.08) \times 10^6$
C (μF cm^{-2})	38.38	5.98	4.92	4.49
τ (s)	1.78	8.91	17.47	19.58
χ^2	4.73×10^{-4}	7.56×10^{-4}	1.92×10^{-3}	1.03×10^{-3}

excellent corrosion stability when immersed in the 5 wt.% H_2SO_4 solution over 7 days, which is further substantiated by SEM observations. As shown in Fig. 9a and b, the corroded surfaces of two Nb-containing Ti$_5$Si$_3$ nanocrystalline coatings are very smooth and devoid of localized corrosion attack. Similarly, the impedance response of the uncoated Ti–6Al–4V substrate shows no obvious difference before and after immersion for 7 days in 5 wt.% H_2SO_4 solution. As shown in Fig. 9c, the uncoated Ti–6Al–4V substrate has undergone some degree of corrosive damage, showing $\alpha + \beta$ two-phase lamellar structure, often exposed by metallographic etching. The impedance spectra of the

Fig. 8. (a) Nyquist and (b) Bode plots of the two Nb-containing Ti$_5$Si$_3$ nanocrystalline coatings, the Ti$_5$Si$_3$ nanocrystalline coating and the uncoated Ti–6Al–4V substrate after immersion in a naturally aerated 5 wt.% H_2SO_4 solution for 7 days. Symbols are experimental data, and solid lines are fitting results.

above three specimens can be fitted with the equivalent circuit model shown in Fig. 7 and the circuit parameters are summarized in Table 4. However, for the Ti$_5$Si$_3$ nanocrystalline coating, the impedance spectrum is distinctly different from the equivalent circuit model shown in Fig. 7. The magnified inset in Fig. 8a reveals that, after immersion for 7 days in 5 wt.% H_2SO_4 solution, the Nyquist plot of the Ti$_5$Si$_3$ nanocrystalline coating shows a depressed semicircle at high frequencies, together with a straight line with a slope of roughly 45° at low frequencies. The former represents the charge transfer-controlled reaction, whereas, the latter reflects a diffusion-controlled mechanism, also known as Warburg diffusional behavior [42]. Furthermore, two time constants are well distinguished in the Bode plot, implying the existence of defects in the coating surface [33]. As shown in Fig. 9d, a pit with diameter ~15 μm is observed and, moreover, coating delamination is also visible around the pit edges. Therefore, the equivalent circuit presented in Fig. 10 was applied to model the impedance data of the Ti$_5$Si$_3$ nanocrystalline coating after immersion for 7 days in 5 wt.% H_2SO_4 solution. A perfect fit to the experimental data indicates that the proposed equivalent circuit is appropriate to evaluate quantitatively the corrosion resistance of the Ti$_5$Si$_3$ nanocrystalline coating. In this circuit, R_s is the solution resistance, R_1 is the coating resistance, R_2 is the charge transfer resistance, CPE$_1$ and CPE$_2$ are the constant phase elements modeling the capacitance of the coating and electrical double layer, respectively, and W is the Warburg impedance, accounting for the semi-infinite diffusion process of the charging species [48]. The diffusion process is regarded to be associated with the accumulation of corrosion products in the pores of the coatings, resulting in the formation of infinite length diffusion paths [42]. From the circuit parameter values shown in Table 4, it is obvious that, after the immersion for 7 days in a 5 wt.% H_2SO_4 solution, the Ti$_5$Si$_3$ nanocrystalline coating shows a more than two orders of magnitude decrease in the polarization resistance ($R_1 + R_2$), signaling the catastrophic deterioration of the coating. For the Ti$_{56.2}$Nb$_{6.3}$Si$_{37.5}$ and Ti$_{50.0}$Nb$_{12.5}$Si$_{37.5}$ nanocrystalline coating, the polarization resistance (R_p) is, respectively, 1.46 and 2.21 times larger than the original value, which may be related to the thickening of the passive film. In the case of the uncoated Ti–6Al–4V substrate, the values of polarization resistance are comparable before and after the immersion tests.
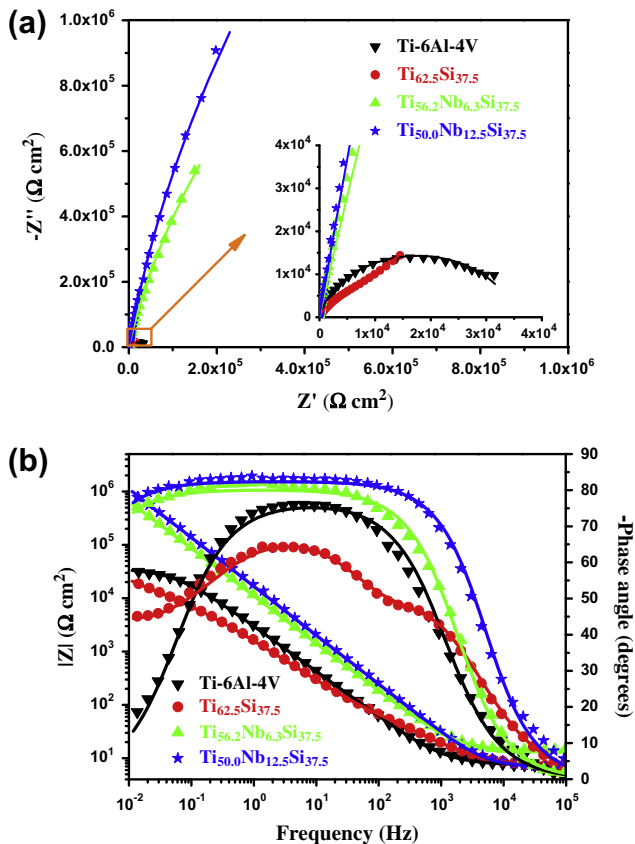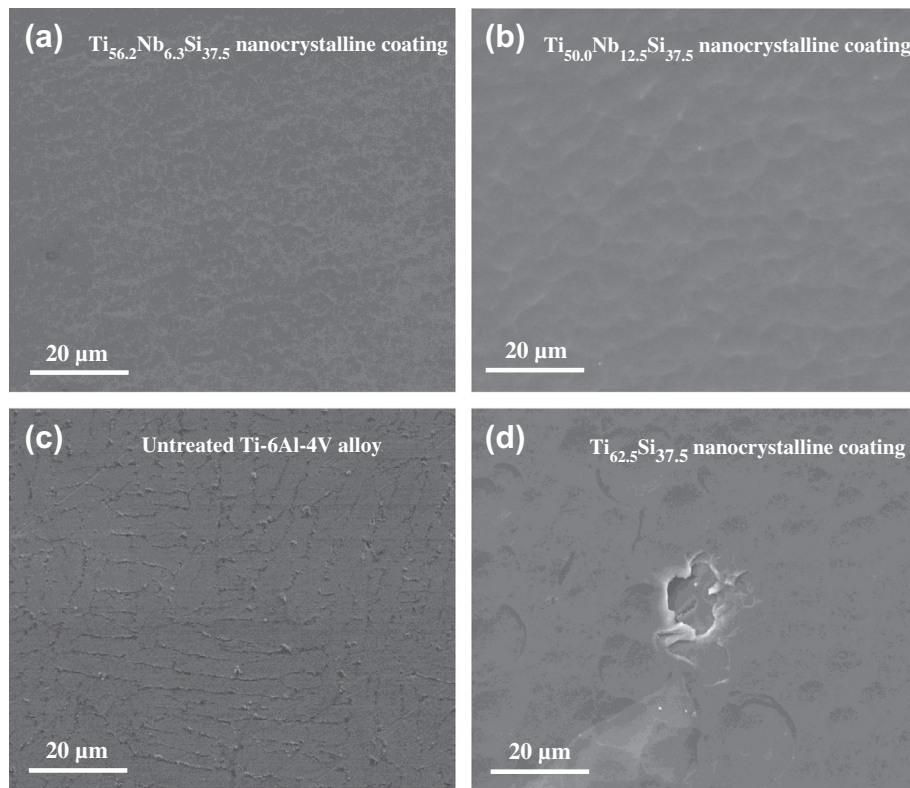
Fig. 9. SEM surface morphologies of (a) the $Ti_{56.2}Nb_{6.3}Si_{37.5}$ nanocrystalline coating, (b) the $Ti_{50.0}Nb_{12.5}Si_{37.5}$ nanocrystalline coating, (c) the uncoated Ti–6Al–4V alloy and (d) the $Ti_{62.5}Si_{37.5}$ nanocrystalline coating after immersion in a naturally aerated 5 wt.% H_2SO_4 solution for 7 days.

4. Discussion

Alloying has been used frequently as an effective strategy to enhance a material's corrosion resistance, in part based on the fact that the minor alloying elements can migrate into passive films and modify their properties [22,49–52]. It is worth noting that niobium (Nb) possesses high passivating ability in diverse aqueous environments [53–55] and has been selected, for example, as an alloying element to improve the corrosion resistance of titanium alloys [22,56,57]. In the present work, Nb was added to the Ti_5Si_3 nanocrystalline coating as an alloying element, which markedly improved the corrosion resistance of the resultant coatings, as shown by the results of potentiodynamic polarization and EIS measurements. For a better understanding of the beneficial effect of Nb additions on the corrosion performance of the coatings, the chemical composition, stability and electronic properties of the passive films formed on Ti_5Si_3 and $Ti_{50.0}Nb_{12.5}Si_{37.5}$ nanocrystalline coatings were further characterized by XPS, potentiostatic polarization and Mott–Schottky analysis.

4.1. Influence of Nb addition on the stability of passive film

The compactness of the passive film is one of the key factors that influence the stability of a passive film. A higher compactness imparts the passive film with a greater protective ability to obstruct the permeation of aggressive

ions into the film [43]. In order to analyze the compactness of the passive film, the variation in current density with time for each specimen after cathodic reduction was measured at a fixed potential (0.80 V_{SCE}). According to the literature [58], if the contribution of the double layer charge is negligible, the initial decrease in current density can be related to the growth of a passive film on the electrode surface. The current density decreases with time according to the following relationship [59]:

$$i = 10^{-(A+klgt)} \tag{3}$$

where i represents the current density, t is time, A is constant, and k represents the slope of the double-log plot for potentiostatic polarization, reflecting the compactness of the passive film; $k = -1$ indicates the formation of a compact, highly protective passive film, while $k = -0.5$ indicates the presence of a porous and diffusion-controlled film. Fig. 11 presents the double-log plots of current density–time for the two coatings and the uncoated Ti–6Al–4V substrate potentiostatically polarized at 0.80 V_{SCE}. As shown in Fig. 11, k values for the passive films grown on the uncoated Ti–6Al–4V substrate, the Ti_5Si_3 and $Ti_{50.0}Nb_{12.5}Si_{37.5}$ nanocrystalline coating are, respectively, −0.70, −0.89 and −0.97, indicating that the compactness of passive films increases in the following sequence: Ti–6Al–4V < Ti_5Si_3 < $Ti_{50.0}Nb_{12.5}Si_{37.5}$. The passive films grown on the two nanocrystalline coatings have superior compactness compared with that formed on the uncoated

Table 4
Equivalent electrical circuit parameters of the investigated specimens after immersion in a naturally aerated 5 wt.% H_2SO_4 solution for 7 days.

Samples	R_s (Ω cm²)	CPE (Ω^{-1} cm⁻² sⁿ)	n	R_p (Ω cm²)	χ^2
Ti–6Al–4V	7.48 ± 0.07	(6.64 ± 0.06) × 10⁻⁵	0.853 ± 0.002	(3.57 ± 0.06) × 10⁴	1.70 × 10⁻³
Ti$_{56.2}$Nb$_{6.3}$Si$_{37.5}$	14.17 ± 0.10	(1.71 ± 0.01) × 10⁻⁵	0.891 ± 0.001	(5.17 ± 0.78) × 10⁶	9.13 × 10⁻⁴
Ti$_{50.0}$Nb$_{12.5}$Si$_{37.5}$	6.86 ± 0.08	(1.07 ± 0.01) × 10⁻⁵	0.916 ± 0.001	(9.62 ± 2.22) × 10⁶	1.82 × 10⁻³

Samples	R_s (Ω cm²)	CPE$_1$ (Ω^{-1} cm⁻² sⁿ)	n_1	R_1 (Ω cm²)	CPE$_2$ (Ω^{-1} cm⁻² sⁿ)	n_2	R_2 (Ω cm²)	W (Ω^{-1} cm⁻² s$^{0.5}$)
Ti$_{62.5}$Si$_{37.5}$	6.97 ± 0.04	(2.13 ± 0.21) × 10⁻⁴	0.720 ± 0.012	25.80 ± 1.82	(1.39 ± 0.02) × 10⁻⁴	0.776 ± 0.004	(1.06 ± 0.05) × 10⁴	(1.68 ± 0.03) × 10⁻⁴

Ti–6Al–4V substrate. These results also demonstrate that the compactness of the passive film on Ti_5Si_3 nanocrystalline coating can be improved by alloying with Nb, which may be attributed to the higher chemical stability and the lower solubility of Nb oxide with respect to TiO_2 in acidic media [57]. The passive film with higher compactness is effective in preventing the penetration of corrosive species into the underlying coating, and thus retards the corrosive damage of the coating.

4.2. Influence of Nb addition on the chemical composition of passive film

Since the chemical composition and the bonding configuration of constituent elements of the passive film are important to its stability and performance, XPS analysis was performed on the surface of the two coatings subjected to the electrochemical treatment. In doing so, a better understanding of the effect of Nb additions on the corrosion resistance of the Ti_5Si_3 coating may be forged. Fig. 12 displays the XPS data obtained from the Ti_5Si_3 and $Ti_{50.0}Nb_{12.5}Si_{37.5}$ nanocrystalline coatings potentiostatically polarized at 0.80 V_{SCE} for 1 h in naturally aerated 5 wt.% H_2SO_4 solution. As shown in Fig. 12a, the XPS spectra over the wide binding energy region for both of the two coatings exhibit peaks for Ti, Si, O and C, including Nb peaks for the Nb-containing Ti_5Si_3 coating. The recorded C 1s spectrum exhibiting a peak at ~284.8 eV possibly arises from a contaminant hydrocarbon layer covering the specimen surface. Fig. 12b–d shows the high-resolution XPS spectra of the two as-deposited coatings, where the experimental data with their respective curve fittings are presented. The Ti 2p spectrum (Fig. 12b) of the Ti_5Si_3 coating presents one spin orbit doublets of Ti 2$p_{1/2}$ and Ti 2$p_{3/2}$ with respective binding energies of 464.3 and 458.6 eV, corresponding to TiO_2 [56]. It is worth mentioning that the binding energies of the Ti 2p peaks for the $Ti_{50.0}Nb_{12.5}Si_{37.5}$ coating shift slightly towards the lower values compared with that of the Ti_5Si_3 coating, presumably owing to the incorporation of Nb into the TiO_2 lattice [60]. The Si 2p spectra (Fig. 12c) show a single peak centered at 103.4 eV in accordance with the published reference values for SiO_2 [49]. The Nb 3d spectrum (Fig. 12d) recorded from the $Ti_{50.0}Nb_{12.5}Si_{37.5}$ coating consists of two peaks with binding energies of 207.2 and 210.0 eV, corresponding to the 3$d_{5/2}$ and 3$d_{3/2}$ components of Nb^{5+}, respectively [53]. The dominant constituent of the passive films formed on the two as-deposited coatings derives from quantitative evaluations of the deconvoluted spectra and the surface composition of the passive films determined using integrated intensities of XPS survey spectra. The results show that, by adding 12.5 at.% Nb into Ti_5Si_3, a decrease in the content of TiO_2 occurs from 54.7 to 43.6 at.%, accompanied by an increase in the SiO_2 concentration from 45.3 to 51.6 at.% together with formation of 4.8 at.% Nb_2O_5. Notably, the passive film formed on the Nb-containing Ti_5Si_3 coating is enriched with higher
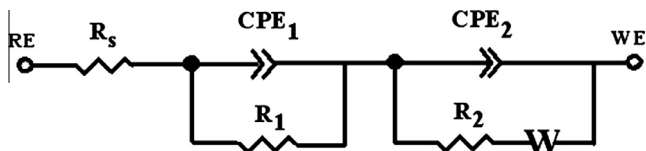
Fig. 10. Equivalent circuit used to model the impedance data of the Ti$_{62.5}$Si$_{37.5}$ nanocrystalline coating after immersion in a naturally aerated 5 wt.% H$_2$SO$_4$ solution for 7 days.

concentrations of SiO$_2$ than that formed on the Ti$_5$Si$_3$ coating, which is presumably due to the addition of Nb. Regarding the role of silicon in the improved corrosion resistance of Si-containing alloys and intermetallics, various explanations, based on the changes in the chemical composition and the electronic properties of the passive films, have been proposed by different authors [49,61,62]. Since SiO$_2$ exhibits a higher dielectric characteristic and chemical stability than TiO$_2$ [49,63], a SiO$_2$-rich passive film formed on a Nb-containing Ti$_5$Si$_3$ nanocrystalline coating is presumed to possess higher capacitive character and may also be responsible for the enhanced compactness.

4.3. Influence of Nb addition on the electronic properties of passive film

In addition to the structural and compositional information garnered above, the electronic properties of the passive film are valuable in an attempt to develop a mechanistic understanding of corrosion in the coating samples. Mott–Schottky analysis based on impedance measurements is a powerful in situ technique for assessing the electronic properties of the passive film. It has been used successfully in the past for the characterization of passive films formed on different passive materials [37,40,64]. According to semiconductor physical theory, the Mott–Schottky relationship expressing the potential dependence of the space charge capacitance C_{sc} of a semiconductor film under depletion condition is described by Eq. (5) [65]:

Fig. 11. Current vs. time plots for the two Ti$_5$Si$_3$ coatings and the uncoated Ti–6Al–4V alloy at 0.80 V_{SCE} in a naturally aerated 5 wt.% H$_2$SO$_4$ solution.

$$\frac{1}{C} = \frac{1}{C_H} + \frac{1}{C_{sc}} \qquad (4)$$

$$\frac{1}{C_{sc}^2} = \frac{2}{\varepsilon_r \varepsilon_0 q N_q}\left(E - E_{fb} - \frac{kT}{q}\right) \qquad (5)$$

where C is the measured capacitance, C_H is Helmholtz capacitance, assumed to be constant with value of 20 μF cm^{-2} [66], ε_r is the dielectric constant of the passive film, ε_0 is the vacuum permittivity (8.854×10^{-14} F cm^{-1}), q is the elementary charge (+e for electrons and −e for holes), N_q is the density of charge carriers (N_d for donors and N_a for acceptors), E is the applied potential, E_{fb} is the flat band potential, k is the Boltzmann constant (1.38×10^{-23} J K^{-1}), and T is the absolute temperature (298 K). The value of kT/q can be neglected, because it is only ~25 mV at room temperature.

Fig. 13 shows the measured Mott–Schottky plots for the passive films formed on the Ti$_{50.0}$Nb$_{12.5}$Si$_{37.5}$ and Ti$_5$Si$_3$ nanocrystalline coatings, as well as on the uncoated Ti–6Al–4V substrate at 0.80 V_{SCE} for 1 h in naturally aerated 5 wt.% H$_2$SO$_4$ solution. All the measured Mott–Schottky plots exhibit a linear region with a positive slope, indicating that the passive films formed on these tested specimens exhibit n-type semiconductor properties. For an n-type semiconducting passive film, the parameter N_q refers to donor density (N_d) in the space charge region, and the donors are usually some positively charged non-stoichiometric point defects, including oxygen vacancies and cation interstitials [50,67]. For the uncoated Ti–6Al–4V substrate and the Ti$_5$Si$_3$ nanocrystalline coating, as shown in Fig. 13a and b, a potential region (at ~−0.20–0.10 V_{SCE}) with approximate constant C_{sc}^{-2} can be identified, reflecting the potential independence of the measured capacitance. This phenomenon has also been observed by other researchers and has been ascribed to different factors [68–70]. For example, Carmezim et al. [68] studied the semiconducting behavior of Cr-oxide films deposited on stainless steels and reported that such a phenomenon originated from the amorphous character of the oxide film. Conversely, Jiang et al. [69] implemented a non-linear fitting method to investigate the semiconducting properties of passive films of Ni-based alloy. They found that an outer p-type hydroxide layer contributed predominantly to the non-linear section in the Mott–Schottky plot. The methodology proposed by Jiang et al. applies to the bipolar passive films with n–p heterojunction structure, as represented by the passive films formed on the various Fe–Cr alloys [69–71]. According to the results of XPS analysis, the passive films formed on the two as-deposited nanocrystalline coatings are a mixture of diverse oxides, such as TiO$_2$, Nb$_2$O$_5$ and SiO$_2$, all of which are characterized by n-type semiconducting properties. Therefore, such a phenomenon occurred in the Mott–Schottky plots is believed to be associated with the amorphous nature of the passive films formed. For the Ti$_{50.0}$Nb$_{12.5}$Si$_{37.5}$ nanocrystalline coating, the absence of the horizontal potential region in the Mott–Schottky plot (Fig. 13c) is attributable to the limitation of the potential window.
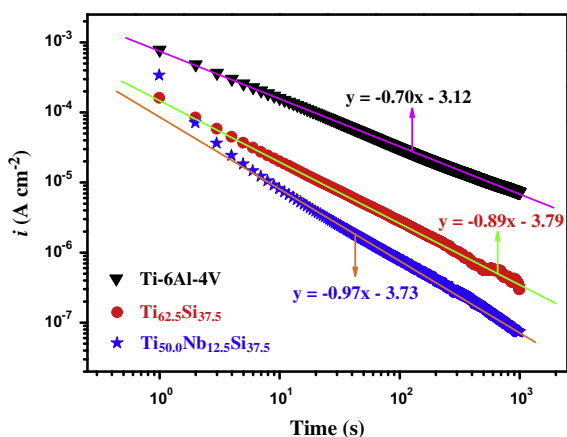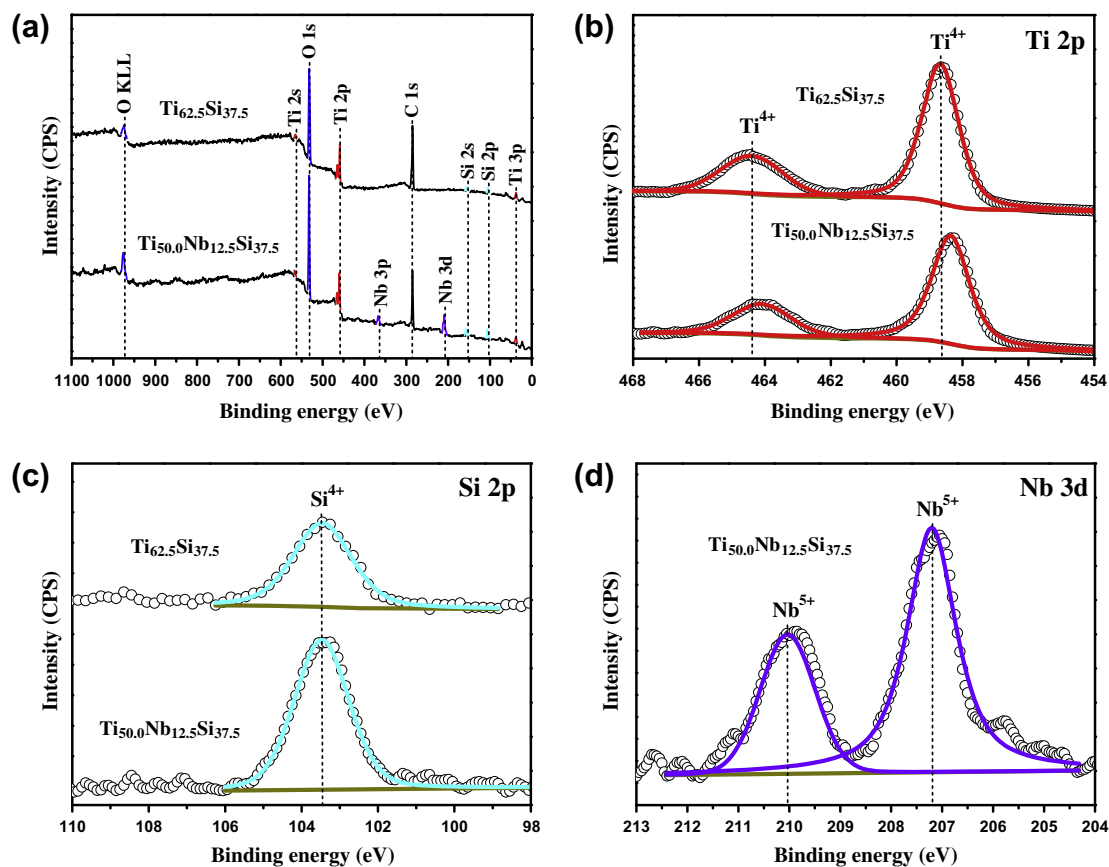
Fig. 12. (a) XPS survey spectra and (b) XPS core level spectra of the Ti 2p, (c) Si 2p and (d) Nb 3d for the passive films formed on the Ti$_5$Si$_3$ and Ti$_{50.0}$Nb$_{12.5}$Si$_{37.5}$ nanocrystalline coatings after potentiostatic polarization at 0.80 V_{SCE} for 1 h in a naturally aerated 5 wt.% H$_2$SO$_4$ solution.

The dielectric constant (ε_r) of the respective passive films formed on the two as-deposited nanocrystalline coatings was determined based on the composition of the passive films derived from the XPS analysis and the mixture rule [72], where values of 60 [64], 41 [54] and 4.34 [64] are taken for pure TiO$_2$, Nb$_2$O$_5$ and SiO$_2$, respectively. The corresponding electrochemical parameters were then calculated and presented in Table 5. It can be seen that the donor density (N_d) is the highest for the passive film developed on the uncoated Ti–6Al–4V alloy (7.27×10^{20} cm^{-3}), followed by the Ti$_5$Si$_3$ (2.84×10^{20} cm^{-3}) and Ti$_{50.0}$Nb$_{12.5}$Si$_{37.5}$ (1.37×10^{20} cm^{-3}) coatings. The significant difference in N_d for the three specimens reflects a pronounced variation in the number of oxygen vacancies and/or cation interstitials in the passive films. It is commonly accepted that the carrier density (N_d or N_a) is closely related to the stability and conductivity of the passive film, which in turn determines the corrosion resistance of the coating material underneath [37,51,71,73]. The higher carrier density is associated with more disordered structure of the passive film, and the lower carrier density signifies a more stable and dielectric passive film. Thus, the Ti$_5$Si$_3$ nanocrystalline coating exhibits a higher passive film stability and, thus, greater corrosion resistance compared with the uncoated Ti–6Al–4V substrate, which is in good agreement with the results of the potentiodynamic polarization

tests (Fig. 5). Furthermore, compared with the Ti$_5$Si$_3$ coating, the donor density of the Ti$_{50.0}$Nb$_{12.5}$Si$_{37.5}$ coating is reduced by ~52%, and such a decrease in N_d stems from the doping effect induced by the substitution of Nb for Ti in TiO$_2$. Owing to the similarity in atomic radii of Nb and Ti, the ionized Nb atoms could be incorporated into the passive film by substituting Ti^{4+} cations as donors, as indicated by the Ti 2p binding energy shift observed in XPS analysis (Fig. 12b). This, in turn, results in the annihilation of oxygen vacancies by charge compensation and makes the passive film less defective with stronger protection [22].

The flat band potential (E_{fb}) is a critical parameter used to determine the positions of the semiconductor energy bands with respect to the redox potentials of electro active ions in the electrolyte. These positions are governed mainly by the charge transfer across the semiconductor/electrolyte interface, the contact potential between semiconductor and electrolyte, and the stability of the semiconductor. According to the energy-band model [74], for a sample covered with an n-type semiconducting passive film, it behaves as a conductor at potentials more negative than the passive film's flat band potential, as the passive film enters an accumulation mode. In contrast, at potentials more positive than E_{fb}, the band bending creates a barrier (space charge layer) to electron transfer, and the sample shows a dielectric
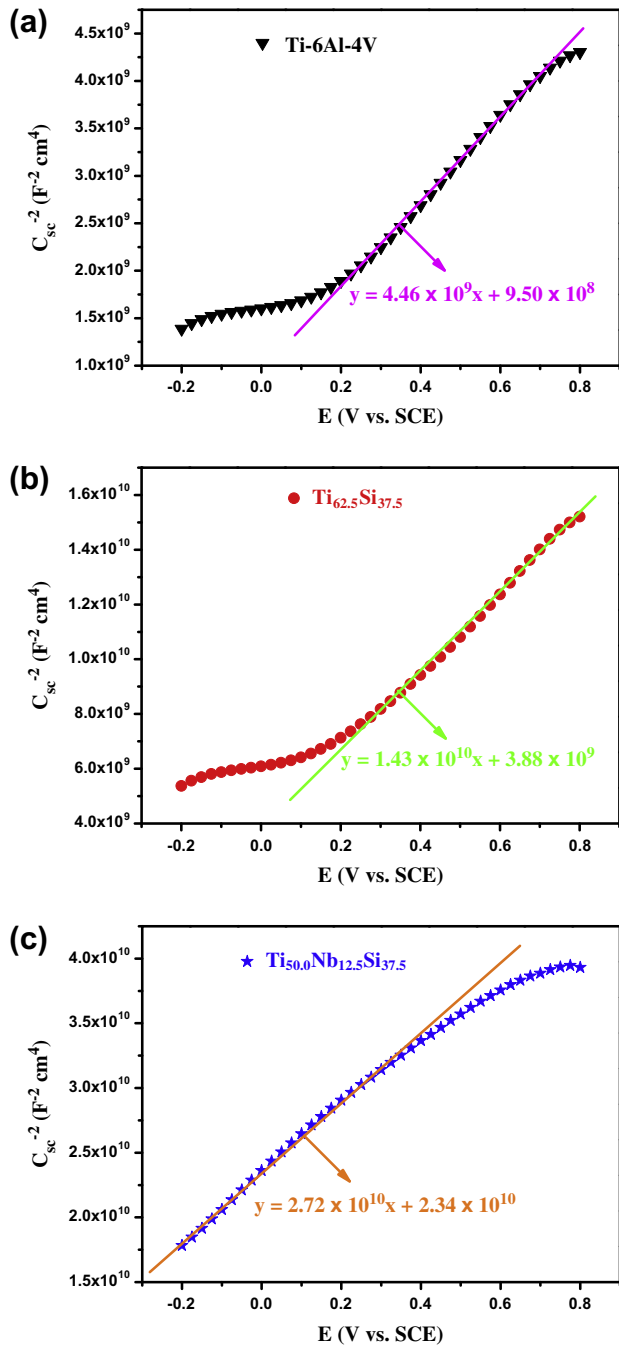
Fig. 13. Mott–Schottky plots of the passive films formed on (a) uncoated Ti–6Al–4V alloy, (b) Ti$_{62.5}$Si$_{37.5}$ nanocrystalline coating and (c) Ti$_{50.0}$-Nb$_{12.5}$Si$_{37.5}$ nanocrystalline coating potentiostatically polarized at 0.80 V_{SCE} for 1 h in a naturally aerated 5 wt.% H$_2$SO$_4$ solution.

Table 5
Electrochemical parameters derived from the Mott–Schottky measurements for the passive films formed on the investigated specimens in a naturally aerated 5 wt.% H$_2$SO$_4$ solution.

Samples	Ti–6Al–4V	Ti$_{62.5}$Si$_{37.5}$	Ti$_{50.0}$Nb$_{12.5}$Si$_{37.5}$
N_d ($\times 10^{20}$ cm^{-3})	7.27	2.84	1.37
E_{fb} (V vs. SCE)	−0.21	−0.27	−0.86
δ_{sc} (nm)	3.03	4.11	6.38

potential of the uncoated Ti–6Al–4V substrate, the Ti$_5$Si$_3$ nanocrystalline coating and the Ti$_{50.0}$Nb$_{12.5}$Si$_{37.5}$ nanocrystalline coating is −0.21, −0.27 and −0.86 V_{SCE}, respectively. As pointed out by Szklarska-Smialowska [77] and Schmidt et al. [78], the oxide film with a lower E_{fb} shows dielectric behavior at a larger potential range and exhibits a higher resistance to pitting. As a result, one might anticipate that the passive film stability would increase in the order: Ti–6Al–4V < Ti$_5$Si$_3$ < Ti$_{50.0}$Nb$_{12.5}$Si$_{37.5}$.

Generally, the thickness of the space charge layer scales directly with that of the passive film. Thus, a thicker passive film would be less prone to dielectric breakdown [80]. Rodríguez and Carranza [81] also suggested that the thickness of the passive film would be equal to that of the space charge layer if the charge were uniformly distributed across the film. The thickness of the space charge layer (δ_{sc}) for an n-type semiconducting passive film can be estimated by the following equation [64]:

$$\delta_{sc} = \left[\frac{2\varepsilon_r\varepsilon_0}{eN_d} \left(E - E_{fb} - \frac{kT}{e} \right) \right]^{1/2} \qquad (6)$$

Table 5 shows that the Ti$_{50.0}$Nb$_{12.5}$Si$_{37.5}$ nanocrystalline coating possesses the largest δ_{sc} (6.38 nm), while the uncoated Ti–6Al–4V substrate has the smallest δ_{sc} (3.03 nm) among the tested specimens. On these grounds, the addition of Nb to Ti$_5$Si$_3$ can promote the formation of a thicker passive film.

5. Conclusions

Two Nb-containing Ti$_5$Si$_3$ nanocrystalline coatings were deposited onto a Ti–6Al–4V substrate. The functional roles of Nb in enhancing the corrosion resistance of the coating were explored. The Nb-containing coatings consist of cauliflower-like structural components with an average diameter of 180 nm, which is composed of petal-like Ti$_5$Si$_3$ grains with an average size of ∼15 nm. The electrochemical properties of the newly developed coating were investigated in naturally aerated 5 wt.% H$_2$SO$_4$ solution using various electrochemical and surface characterization techniques. The following conclusions can be drawn:

(1) Nb atoms can dissolve in Ti$_5$Si$_3$ to occupy Ti sites in the Ti$_5$Si$_3$ lattice, forming a substitutional solid solution and, thus, reduce the residual tensile stress built up in the coating.
(2) Nb alloying can appreciably lower the passive current density and enhance the polarization resistance of the

characteristic. Although a precise determination of the flat band potential is often complicated by the presence of surface states and defects unavoidably connected with the nanometer size of the passive film [75,76], the information on E_{fb} provides useful guides to the understanding of electrochemical behavior. Many researchers have demonstrated that there was an intrinsic relationship between the localized corrosion resistance and the flat band potential of the passive film [77–79]. As shown in Table 5, the flat band

Ti$_5$Si$_3$ nanocrystalline coating in naturally aerated 5 wt.% H$_2$SO$_4$ solution, thus improving its corrosion resistance.

(3) Nb alloying also promotes the enrichment of SiO$_2$ in the passive film formed on the Ti$_5$Si$_3$ coating. This leads to an increase in both the thickness and compactness of the passive film formed on the coating.

(4) The passive films formed on the Ti$_5$Si$_3$ coatings exhibit n-type semiconducting properties, and Nb alloying can markedly reduce the donor densities of the passive film.

(5) After immersion for 7 days in 5 wt.% H$_2$SO$_4$ solution, no significant change in impedance behavior was observed for the Nb-containing Ti$_5$Si$_3$ nanocrystalline coatings, whereas the Ti$_5$Si$_3$ nanocrystalline coating suffered serious corrosion damage, which suggests that Nb alloying may improve the long-term corrosion stability of the Ti$_5$Si$_3$-based nanocrystalline coating in 5 wt.% H$_2$SO$_4$ solution.

Acknowledgment

References

[1] Huang P, Wang F, Xu K, Han Y. Surf Coat Technol 2007;201:5168.
[2] Chen F, Zhou H, Chen C, Xia YJ. Prog Org Coat 2009;64:264.
[3] Kuromoto NK, Simão RA, Soares GA. Mater Charact 2007;58:114.
[4] Galvanetto E, Galliano FP, Fossati A, Borgioli F. Corros Sci 2002;44:1593.
[5] Shokouhfar M, Dehghanian C, Baradaran A. Appl Surf Sci 2011;257:2617.
[6] Yao ZP, Jiang ZH, Sun XT, Xin SG, Li YP. Thin Solid Films 2004;468:120.
[7] Razavi RSh, Salehi M, Monirvaghefi M, Gordani GR. J Mater Process Technol 2008;203:315.
[8] Kuo D-H, Huang K-W. Surf Coat Technol 2001;135:150.
[9] Khaled M, Yilba BS, Shirokoff J. Surf Coat Technol 2001;148:46.
[10] Thair L, Mudali UK, Bhuvaneswaran N, Nair KGM, Asokamani R, Raj B. Corros Sci 2002;44:2439.
[11] Xu J, Lai DH, Xie ZH, Munroe P, Jiang Z-T. J Mater Chem 2012;22:2596.
[12] Xu J, Mao XZ, Xie Z-H, Munroe P. J Phys Chem C 2011;115:18977.
[13] Kishida K, Fujiwara M, Adachi H, Tanaka K, Inui H. Acta Mater 2010;58:846.
[14] Wang H-Y, Lü S-J, Xiao W, Liu G-J, Wang J-G, Jiang Q-C. J Am Ceram Soc 2013;96:950.
[15] Williams JJ, Kramer MJ, Akinc M. J Mater Res 2000;15:1780.
[16] Rodrigues G, Nunes CA, Suzuki PA, Coelho GC. Intermetallics 2006;14:236.
[17] Thom AJ, Meyer MK, Kim Y, Akinc M. In: Ravi VA, Srivatsan TS, Moore JJ, editors. Processing and fabrication of advanced materials III. Warrendale (PA): TMS; 1994. p. 413.
[18] Zhang LT, Wu JS. Scripta Mater 1998;38:307.
[19] Ikarashi Y, Ishizaki K, Nagai T, Hashizuka Y, Kondo Y. Intermetallics 1996;4:S141.
[20] Xu J, Liu LL, Lu XL, Jiang SY. Electrochem Commun 2011;13:102.
[21] Yu SY, Scully JR. Corrosion 1997;53:965.
[22] Metikoš-Huković M, Kwokal A, Piljac J. Biomaterials 2003;24:3765.
[23] Cao LZ, Shen J, Chen NX. J Alloy Compd 2002;336:18.
[24] Perdew JP, Burke K, Ernzerhof M. Phys Rev Lett 1996;77:3865.
[25] Monkhorst HJ, Pack JD. Phys Rev B 1977;16B:1748.
[26] Fischer TH, Almlof J. J Phys Chem 1992;96:9768.
[27] Hill R. Proc Phys Soc Lond 1952;65:350.
[28] Zhang L, Wu J. Acta Mater 1998;46:3535.
[29] Zhang S, Xie H, Zeng X, Hing P. Surf Coat Technol 1999;122:219.
[30] Thornton JA, Hoffman DW. Thin Solid Films 1989;171:5.
[31] Sriraman KR, Brahimi S, Szpunar JA, Osborne JH, Yue S. Electrochim Acta 2013;105:314.
[32] Hauert R, Thorwarth K, Thorwarth G. Surf Coat Technol 2013;233:119.
[33] Li L, Niu E, Lv GH, Zhang XH, Chen H, Fan SH, et al. Appl Surf Sci 2007;253:6811.
[34] Díaz B, Härkönen E, Światowska J, Maurice V, Seyeux A, Marcus P, et al. Corros Sci 2011;53:2168.
[35] Li DJ, Hassani S, Poulin S, Szpunar JA, Martinu L, Klemberg-Sapieha JE. J Appl Phys 2012;111:043512.
[36] Potucek PK, Rateick RG, Birss VI. J Electrochem Soc 2006;153:B304.
[37] Yahia SAA, Hamadou L, Kadri A, Benbrahim N, Sutter EMM. J Electrochem Soc 2012;159:K83.
[38] Jüttner K. Electrochim Acta 1990;35:1501.
[39] Ameer MA, Fekry AM, Heakal FE-T. Electrochim Acta 2004;50:43.
[40] Sun A, Franc J, Macdonald DD. J Electrochem Soc 2006;153:B260.
[41] Rincón ME, Martínez MW, Miranda-Hernández M, González I. J Electrochem Soc 2002;149:E317.
[42] Grips VKW, Selvi VE, Barshilia HC, Rajam KS. Electrochim Acta 2006;51:3461.
[43] Liu LL, Xu J, Xie Z-H, Munroe P. J Mater Chem A 2013;1:2064.
[44] Karimi S, Alfantazi AM. J Electrochem Soc 2013;160:C206.
[45] Krawiec H, Vignal V, Schwarzenboeck E, Banas J. Electrochim Acta 2013;104:400.
[46] Brug GJ, Van Den Eeden ALG, Sluyters-Rehbach M, Sluyters JH. J Electroanal Chem 1984;176:275.
[47] Petrossians A, Whalen JJ, Weiland JD, Mansfeld F. J Electrochem Soc 2011;158:D269.
[48] Guo RQ, Zhang C, Chen Q, Yang Y, Li N, Liu L. Corros Sci 2011;53:2351.
[49] Jiang ZL, Dai X, Middleton H. Mater Sci Eng B 2011;176:79.
[50] Kang JQ, Yang YF, Jiang X, Shao HX. Corros Sci 2008;50:3576.
[51] Lee J-B, Yoon S-I. Mater Chem Phys 2010;122:194.
[52] Urquidi M, Macdonald DD. J Electrochem Soc 1985;132:555.
[53] Wang W, Mohammadi F, Alfantazi A. Corros Sci 2012;57:11.
[54] Li DG, Wang JD, Chen DR. Electrochim Acta 2012;60:134.
[55] Qin CL, Zhang W, Asami K, Kimura H, Wang XM, Inoue A. Acta Mater 2006;54:3713.
[56] Vasilescu C, Drob SI, Neacsu EI, Mirza Rosca JC. Corros Sci 2012;65:431.
[57] Yu SY, Scully JR, Vitus CM. J Electrochem Soc 2001;148:B68.
[58] Galvele JR, Torresi RM, Carranza RM. Corros Sci 1990;31:563.
[59] Hassan HH. Electrochim Acta 2005;51:526.
[60] Zhu JF, Deng ZG, Chen F, Zhang JL, Chen HJ, Anpo M, et al. Appl Catal B: Environ 2006;62:329.
[61] Rosalbino F, Carlini R, Parodi R, Zanicchi G. Electrochim Acta 2012;62:305.
[62] Toor IH. J Electrochem Soc 2011;158:C391.
[63] Pantelides ST, Harrison WA. Phys Rev B 1976;13:2667.
[64] Jovic VD, Barsoum MW. J Electrochem Soc 2004;151:B71.
[65] Morrison SR. Electrochemistry at semiconductor and oxidized metal electrodes. New York: Plenum Press; 1980. p. 127.
[66] Di Quarto F, Di Paola A, Sunseri C. J Electrochem Soc 1980;127:1016.
[67] Macdonald DD. J Electrochem Soc 1992;139:3434.
[68] Carmezim MJ, Simões AM, Figueiredo MO, Da Cunha Belo M. Corros Sci 2002;44:451.

[69] Jiang R-J, Chen C-F, Zheng S-Q, Cui L-S. J Electroanal Chem 2011;658:52.
[70] Escrivà-Cerdán C, Blasco-Tamarit E, García DM, García-Antón J, Guenbour A. Electrochim Acta 2012;80:248.
[71] Ye W, Li Y, Wang FH. Electrochim Acta 2006;51:4426.
[72] Anjana PS, Sebastian MT, Axelsson A-K, Alford NM. J Eur Ceram Soc 2007;27:3445.
[73] Li DG, Wang JD, Chen DR. J Power Sources 2012;210:163.
[74] Oguzie EE, Li JB, Liu YQ, Chen DM, Li Y, Yang K, et al. Electrochim Acta 2010;55:5028.
[75] Sikora E, Sikora J, Macdonald DD. Electrochim Acta 1996;41:783.
[76] Spadavecchia F, Cappeletti G, Ardizzone S, Ceotto M, Falciola L. J Phys Chem C 2011;115:6381.
[77] Szklarska-Smialowska Z. Corros Sci 1999;41:1743.
[78] Schmidt AM, Azambuja DS, Martini EMA. Corros Sci 2006;48:2901.
[79] Harrington SP, Devine TM. J Electrochem Soc 2009;156:C154.
[80] Hakiki NE. Corros Sci 2011;53:2688.
[81] Rodríguez MA, Carranza RM. J Electrochem Soc 2011;158:C221.